

Room temperature plasmon-enhanced InAs_{0.91}Sb_{0.09}-based heterojunction n-i-p mid-wave infrared photodetector

Tobing, Landobasa Yosef Mario; Tong, Jinchao; Qiu, Shupeng; Zhang, Dao Hua; Unil Perera, A. G.

2018

Tong, J., Tobing, L. Y. M., Qiu, S., Zhang, D. H., & Unil Perera, A. G. (2018). Room temperature plasmon-enhanced InAs_{0.91}Sb_{0.09}-based heterojunction n-i-p mid-wave infrared photodetector. *Applied Physics Letters*, 113(1), 011110-. doi:10.1063/1.5018012

<https://hdl.handle.net/10356/88527>

<https://doi.org/10.1063/1.5018012>

© 2018 The Author(s). All rights reserved. This paper was published by AIP Publishing in *Applied Physics Letters* and is made available with permission of The Author(s).

Downloaded on 13 Mar 2024 14:52:22 SGT

Room temperature plasmon-enhanced InAs_{0.91}Sb_{0.09}-based heterojunction *n-i-p* mid-wave infrared photodetector

Jinchao Tong,¹ Landobasa Y. M. Tobing,¹ Shupeng Qiu,¹ Dao Hua Zhang,^{1,a)} and A. G. Unil Perera²

¹*School of Electrical and Electronic Engineering, Nanyang Technological University, Nanyang Avenue, Singapore 639798*

²*Department of Physics and Astronomy, Georgia State University, Atlanta, Georgia 30303, USA*

(Received 2 December 2017; accepted 19 June 2018; published online 5 July 2018)

Middle wavelength infrared (MWIR) photodetectors have a wide range of applications, but almost all of them operate at low temperature due to the limit of materials and device structures. The capability of plasmonic structures to localize electromagnetic wave on the deep subwavelength scale provides the possibility for MWIR photodetectors operating at room temperature. Here, we report a high sensitivity room temperature MWIR photodetector which is an InAs_{0.91}Sb_{0.09}-based heterojunction *n-i-p* photodiode integrated with a Au-based two-dimensional subwavelength hole array (2DSHA). A room temperature detectivity of $0.8 \times 10^{10} \text{ cm Hz}^{1/2} \text{ W}^{-1}$ and a response time of 600 ns are achieved. The non-cooling high performance of 2DSHA-InAs_{0.91}Sb_{0.09} based heterojunction photodetectors will make their applications easier, broader, and economic. *Published by AIP Publishing.* <https://doi.org/10.1063/1.5018012>

Middle wavelength infrared (MWIR, 3–5 μm) photodetectors have various applications in security, communication, medical diagnostics, and remote sensing. Most of the MWIR photodetectors operate at low temperature due to limited detection performance. Mercury cadmium telluride (HgCdTe/MCT) photodetectors have taken a dominant position in this wavelength range, but they come with practical constraints of non-uniformity of the material due to high Hg pressure and the need for a thick absorption layer (several microns) due to its low absorption coefficient. PbSe photoconductors can work at room temperature but usually under larger bias and with lower speed.¹ In the past few decades, Antimonide (Sb) based III-V materials have shown great promise for MWIR focal planar arrays (FPAs) owing to their good uniformity in material growth and well established fabrication techniques.^{2–9} However, due to the narrow bandgap properties and small absorption in the 3–5 μm range, these photodetectors typically possess a thick absorption layer and suffer from large dark current, thus limiting their room temperature applications.

It is well known that the main challenge in designing a photodiode lies in the inherent trade-off between responsivity and thickness of the absorption layer (device speed). Higher responsivity is achieved in a thicker absorption layer, but at the expense of longer transit time and thus slower response. Recently, surface plasmon polaritons (SPPs) on the subwavelength scale have attracted tremendous attention as they have multitudinous applications, depending on the dimension of the plasmonic structures and operation frequency.^{10–14} The exceptional ability of plasmonic structures to confine light in extremely small volume has proved useful in improving the performances of solar cells and photodetectors in the visible and near infrared wavelength range. For MWIR, plasmonic-grating enhanced nBn photodetectors have been reported at 120 K.⁴ A Ge/Si quantum dot (QD) photodetector integrated

with a circular hole array has also been reported at 78 K.¹⁵ For the 5–10 μm range, InAs QDs^{16–18} integrated with plasmonic structures have been developed, showing potential for sensitive large FPAs but still at low temperatures.

In this work, we integrate a gold two-dimensional subwavelength square hole array (2DSHA) with an InAs_{0.91}Sb_{0.09} based heterojunction *n-i-p* photodiode for MWIR photodetection with excellent room temperature performances. With proper design, a detectivity of $0.8 \times 10^{10} \text{ cm Hz}^{1/2} \text{ W}^{-1}$ with an impulse response of 600 ns at room temperature has been demonstrated.

Figure 1 shows the schematic of the room temperature 2DSHA-hetero *n-i-p* MWIR photodetector which is an integration of a 2DSHA and an InAs_{0.91}Sb_{0.09} based heterojunction *n-i-p* photodiode. The *n-i-p* structure is epitaxially grown on an n-type GaSb substrate (Te: $1.5 \times 10^{18} \text{ cm}^{-3}$). It consists of a 1 μm thick intrinsic absorptive InAs_{0.91}Sb_{0.09} (nonintentionally doped) layer sandwiched by 20 nm thick n-type (Si: $1 \times 10^{18} \text{ cm}^{-3}$) and p-type (Be: $1 \times 10^{18} \text{ cm}^{-3}$) Al_{0.15}In_{0.85}As_{0.9}Sb_{0.1} layers. A p-type (Be: $1 \times 10^{18} \text{ cm}^{-3}$) GaSb buffer layer (1 μm) is used as the bottom contact layer followed by a 40 nm p-doped (Be: $2 \times 10^{18} \text{ cm}^{-3}$) Al_{0.42}Ga_{0.58}Sb layer. To reduce dark current, some wide bandgap layers are introduced in this heterojunction. As shown in the schematic band diagram of this structure (left-bottom inset), the p-doped Al_{0.42}Ga_{0.58}Sb layer with a wide bandgap is used to reduce the dark current of electrons from the p side. The p-doped Al_{0.15}In_{0.85}As_{0.9}Sb_{0.1} is inserted to limit type II electron-hole transitions between the Al_{0.42}Ga_{0.58}Sb and InAs_{0.91}Sb_{0.09} layers.

The purpose of having only a 20 nm thick top n-type layer is to ensure more SPPs to interact with the active intrinsic absorptive InAs_{0.91}Sb_{0.09} layer. The top and bottom ohmic contacts are 15 nm thick titanium (Ti) followed by 200 nm thick gold (Au). The 300- μm sized square mesas are defined by wet etching, followed by deposition of the

^{a)}Email: EDHZHANG@ntu.edu.sg

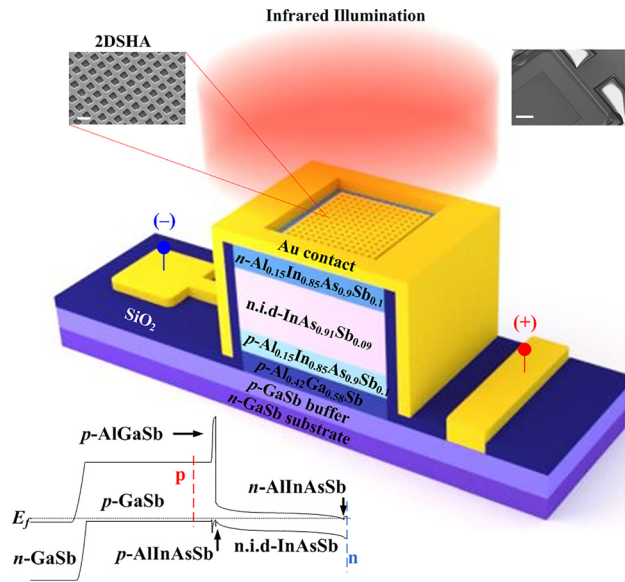


FIG. 1. Design of the 2DSHA-hetero *n-i-p* photodetector for enhanced mid-wave infrared photodetection. Inset: SEM images of the 2DSHA (left) and top view of the 2DSHA-hetero *n-i-p* photodetector (with an angle of 30°). The scale bars are 1 μm and 50 μm , respectively. Left-bottom is the schematic band diagram of this heterojunction. p and n indicate the positions for metal electrodes.

350 nm SiO_2 passivation layer (PECVD) to reduce the surface leakage current and protect the mesas. In our work, the metallic 2DSHA structure is fabricated on top of the $\text{InAs}_{0.91}\text{Sb}_{0.09}$ based *n-i-p* by electron beam lithography (EBL), followed by metal evaporation and a standard lift-off process. The metal surface consists of a 3 nm thick Ti adhesion layer and 70 nm thick Au. The thickness of gold is chosen to be 70 nm which is much more than the skin depth¹⁹ (4.3–10.7 nm for gold for 1–6 μm , $\delta_s = \sqrt{\rho/(\pi f \mu)}$, where ρ is the resistivity, f is the frequency, and μ is the relative permeability) to avoid direct transmission through the metal film. In fabrication, the 2DSHA and reference *n-i-p* photodiodes have undergone the same technical process except for the final step where the metals for 2DSHA are kept for plasmonic devices.

The $\text{InAs}_{0.91}\text{Sb}_{0.09}$ based heterojunction photodiode is chosen here as it has reasonable detectivity at high temperatures and the materials have high stability and are easy for larger area arrays. In general, the responsivity and device speed of the *n-i-p* structure depend on the thickness of the intrinsic layer. Higher speed can be achieved by employing a narrower intrinsic layer at the expense of reduced responsivity, while large responsivity needs a thick intrinsic layer at an expense of longer response time. This trade-off can be overcome by incorporating an Au 2DSHA to the heterojunction *n-i-p* photodiode with a thin intrinsic layer as it provides strong light confinement near the metal-dielectric interface.

In the 2DSHAs, the interaction between light and the surface plasmons obeys momentum conservation given by

$$k_{\text{spp}} = |k_x \pm G_{ij}| = |k_0 \sin \theta \pm iG_x \pm jG_y|, \quad (1)$$

where $k_0 \sin \theta$ is the in-plane incident wave vector and $G_x = G_y = 2\pi/p$ are the reciprocal lattice vectors. k_{spp} is the wave vector of the SPP at the gold-dielectric interface, which

can be expressed as $k_{\text{spp}} = k_0 \sqrt{\epsilon_m \epsilon_d / (\epsilon_m + \epsilon_d)}$.²⁰ At normal incidence ($\theta = 0$), for the Au 2DSHA integrated on top of the sample with a hole period p , the surface plasmon resonance (SPR) wavelengths are given by²⁰

$$\lambda_{ij} = \frac{p}{\sqrt{i^2 + j^2}} \text{Re} \left\{ \left[\frac{\epsilon_m \epsilon_d}{\epsilon_m + \epsilon_d} \right]^{1/2} \right\}, \quad (2)$$

where (i, j) are the set of integers denoting the mode orders in x - and y -directions, and $\epsilon_m(\epsilon_d)$ is the permittivity of the metal (semiconductor). The permittivity of our sample in the wavelength range of interest is ~ 15.1 (the imaginary part is much smaller than the real part)²¹ while the permittivity of gold can be expressed by the Drude model²²

$$\epsilon_m(\omega) = \epsilon_\infty - \frac{\omega_p^2}{\omega(\omega + i\omega_\tau)}, \quad (3)$$

where $\epsilon_\infty = 1$ is the high frequency dielectric constant, $\omega_p = 1.37 \times 10^{16}$ rad/s is the plasma frequency, and $\omega_\tau = 4.07 \times 10^{13}$ rad/s is the collision frequency. Combining Eqs. (2) and (3), for the 2DSHA metallic structures with $p = 900$ nm, the SPR wavelength can be deduced as 3.5 μm for the fundamental plasmon mode (λ_{10} or λ_{01}) at normal incidence, which is located around the peak photocurrent response of the $\text{InAs}_{0.91}\text{Sb}_{0.09}$ based heterojunction *n-i-p* photodiode. At plasmonic resonance, the confinement of SPP waves inside dielectric medium can be described by the SPP penetration depth (δ_d)²³

$$\delta_d = \frac{1}{k_0} \left| \frac{\epsilon'_m + \epsilon_d}{\epsilon_d^2} \right|^{1/2}, \quad (4)$$

where ϵ'_m is the real permittivity of the gold, ϵ_d is the permittivity of the *n-i-p* sample, and k_0 is the wavevector in the free space. The penetration depth of the surface plasmons in the $\text{InAs}_{0.91}\text{Sb}_{0.09}$ based heterojunction *n-i-p* sample at 3.5 μm is found to be $\sim 1 \mu\text{m}$. This serves as the guide for choosing the thickness of the intrinsic absorption layer in our *n-i-p* devices. In experiments, we also fabricated other 2DSHA hetero *n-i-p* devices with hole periods of $p = 550$, 1280, and 1550 nm for comparison. For all the 2DSHAs, the width of the square hole is close to half of p to give better performance.¹⁶

Figure 2 shows the photocurrent spectra (measured by FTIR with an MWIR focus lens) of the $\text{InAs}_{0.91}\text{Sb}_{0.91}$ based heterojunction *n-i-p* (black curves) and the 2DSHA-hetero *n-i-p* (red curves) devices under zero bias, measured at room temperature (293 K) and $T = 77$ K, respectively. For room temperature operation, the $\text{InAs}_{0.91}\text{Sb}_{0.09}$ based heterojunction *n-i-p* photodiode, which will then be referred to as “the reference,” is observed to exhibit broadband response from about 2 μm to 5 μm with a photocurrent peaked at a wavelength of about 3.5 μm . When temperature is decreased to 77 K, the cutoff wavelength is shifted from 5 μm to about 4 μm due to bandgap broadening of the $\text{InAs}_{0.91}\text{Sb}_{0.09}$ layer. At 77 K, the photocurrents are much larger than those at room temperature due to the increased carrier mobility (increased carrier velocity). The absorptions at about 2.7 μm , 3.3 μm , and 4.3 μm by the environmental air are also observable in the photocurrent spectra of both temperatures.

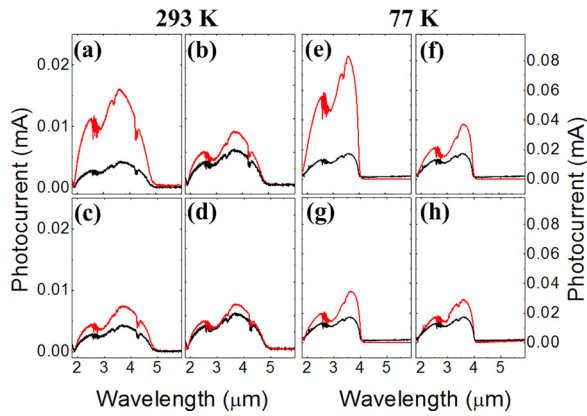


FIG. 2. Room temperature photocurrent spectra of 2DSHA-hetero *n-i-p* photodetectors with periods of (a) 900 nm, (b) 550 nm, (c) 1280 nm, and (d) 1550 nm at zero bias. (e)–(h) Photocurrent spectra at 77 K and zero bias for the devices corresponding to (a)–(d), respectively.

It is noted that all the four 2DSHA-hetero *n-i-p* photodetectors show obvious photocurrent enhancement although the one with the period of 900 nm shows the highest. Specifically, the average enhancement factors are in the range of 3–4 \times for the 2DSHA-hetero *n-i-p* photodetector with $p = 900$ nm and 1–2 \times for the other three photodetectors with $p \neq 900$ nm. As SPR occurs, the optical electrical field (light density) becomes very large especially at around the interface between the metal and the dielectric. To gain insights into the enhanced electrical field, we present numerical simulations (FDTD) for the 2DSHA structures in Fig. 3. The electric field enhancement factors, defined as $B = |E_{x,int}/E_{x,in}|^2$, at $\lambda_0 = 3.5 \mu\text{m}$ and the detuning $[\lambda_{\text{spp}}(i,j) - \lambda_0]$ of the fundamental and high order SPP modes from $\lambda_0 = 3.5 \mu\text{m}$ as a function of hole period of the 2DSHAs are shown in Fig. 3(a). It is clearly seen that maximum field enhancement is obtained when the fundamental resonance matches λ_0 at $p = 900$ nm, and field enhancements in other hole periods also exist due to the contributions from different plasmonic modes. The detuning of the fundamental SPP mode from $\lambda_0 = 3.5 \mu\text{m}$ also has the smallest value when the period $p = 900$ nm. The numerically calculated electric field enhancements of the periodic metal hole array for the 2DSHA with $p = 900$ nm are also shown in Fig. 3(b), where the electric field values are taken from the hot-spot point (for a unit cell, $x = p/2$, $y = 0$, and $z = 0$) with the position indicated in the inset. It is obvious that in addition to the fundamental mode, other higher order plasmonic modes of the 2DSHA also contribute to the field enhancement.

Ideally, if the enhancement occurs due to strong light confinement near the metal-dielectric interface at resonance only, it then follows that the enhancement should be within a narrow wavelength range around those resonance modes. However, this is not the case as enhancements are observed over a broad wavelength range. This broadband character mainly comes from the continually distributed incident angles in the FTIR measurements (mainly from the focus lens). To gain a further insight into this, the SPRs of the 2DSHAs have been separately demonstrated by measuring the reflectance spectra on both this hetero *n-i-p* sample and Si substrates [Fig. 4(a)]. The SPR modes (marked fundamental modes as examples) on Si show obvious blue-shift

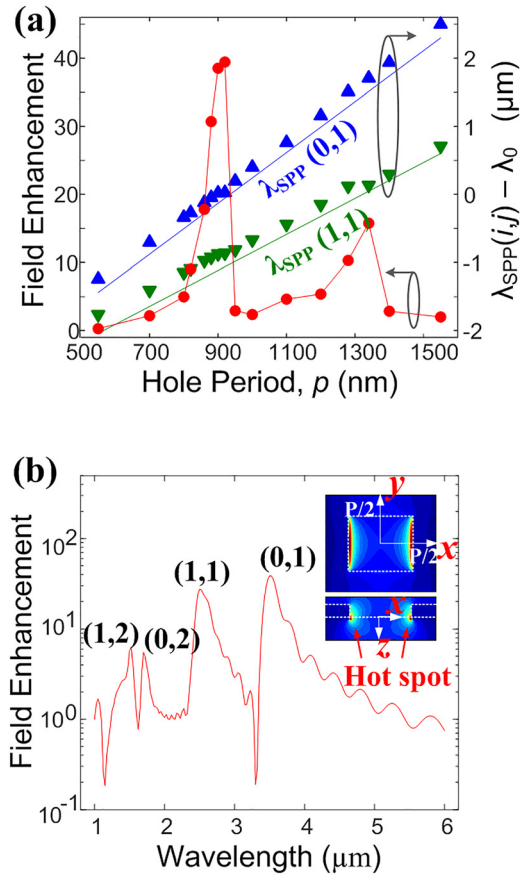


FIG. 3. Field enhancement in the 2DSHAs. (a) Field enhancement factors at $\lambda_0 = 3.5 \mu\text{m}$ and the detuning of fundamental and higher order SPP modes from $\lambda_0 = 3.5 \mu\text{m}$ as a function of hole period. The theoretical results (solid lines) are in agreement with those obtained from FDTD simulations (triangle markers). (b) Electric field enhancement spectrum of the 2DSHA with $p = 900$ nm at the indicated position [for a unit cell $x = p/2$, $y = 0$, and $z = 0$ (metal-semiconductor interface)].

compared to those on hetero *n-i-p* samples as the permittivity of Si (11.8) is smaller than that (15.1) of the hetero InAsSb *n-i-p* sample [abide by Eq. (2)]. The measured broadband reflection spectra can be primarily ascribed to the continually distributed incident angles up to about 30° from the condenser in the experimental set-up (36 \times objective lens (NA = 0.5)). According to Eq. (1), the oblique incidence will lead to splitting and shifting for those SPR modes. To verify, we simulated reflectance spectra of the 2DSHAs with $p = 900$ nm on the hetero *n-i-p* sample at different incident angles as an example [Fig. 4(b)]. It is observed that the SPRs are split and shifted while the incidence angle deviates from normal incidence (0°) to other incidence angles, which is in good agreement with Eq. (1) and other reports.^{15,16,20,24} The averaged reflectance spectrum from 0° to 30° (assuming uniform distribution for qualitative description), also presented in Fig. 4(b), exhibits broadband character, which is in agreement with the measured counterpart. The broadband reflection spectrum corresponds to a broadband transmission spectrum as they are correlated by $R = 1 - T$. Figure 4(c) shows the transmission spectrum of the 2DSHAs with $p = 900$ nm, extracted by $1 - R$. As the continually distributed incident angles in the photocurrent measurement system exist, the broadband transmission spectrum of the 2DSHAs will generate electron-hole pairs over a wide spectrum,

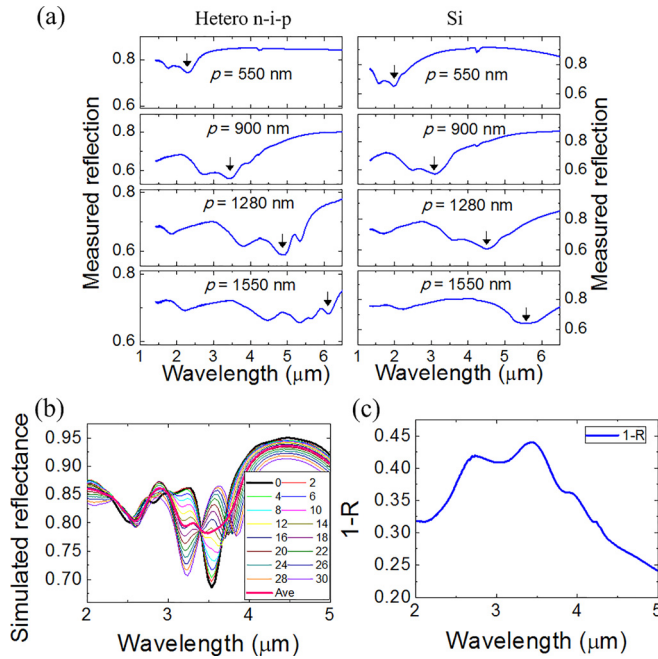


FIG. 4. (a) Measured reflectance spectra of 2DSHAs with different hole periods fabricated on the hetero *n-i-p* (left) and Si (right) samples, respectively. (b) Simulated reflectance spectra of 2DSHA with $p = 900$ nm on the hetero InAsSb *n-i-p* substrate for incident angles from 0° to 30° . The bold pink line is the averaged reflectance spectrum (assuming uniform distribution). (c) The 1-R spectrum of 2DSHA with $p = 900$ nm on the hetero InAsSb *n-i-p* substrate.

resulting in broadband enhancement in photocurrent as shown in Fig. 2. Other factors, such as localized surface plasmons (LSPs), Fabry-Perot (FP) resonance, and prolonged light path can also contribute to the photocurrent enhancements,^{25,26} but their contributions are not significant in our case.

Finally, we used a 700°C blackbody radiation source to characterize the responsivity and detectivity of the 2DSHA-hetero *n-i-p* photodetector with $p = 900$ nm and the reference at room temperature under biased voltages from -350 mV to 350 mV. The room temperature responsivities [$R_i = I_s/P$, where I_s is the signal current and P is incident radiation power on the detector calibrated by a standard power meter (OPHIR PHOTONICS)] of the two devices are presented in Fig. 5(a). As shown, the photoresponses of both devices increase with the increasing reverse voltage owing to the increased electric field (increased carrier velocity), demonstrating that the photocurrent mainly comes from the drifting of photon-excited carriers.²⁷ It is found that the responsivity of the 2DSHA-hetero *n-i-p* photodetector increases when the biased voltage varies from positive to negative and tends to saturate at about -150 mV with a value of 0.85 A/W, as compared to 0.15 A/W for the reference at the same bias. It is noted here that the responsivity of the reference device is saturated at around -350 mV with a value of only 0.3 A/W, while that of the plasmonic device is saturated at about -150 mV with a much larger value. As the current-voltage curves [inset of Fig. 5(a)] confirm that the plasmonic and reference devices have similar dark current characteristics, the difference in the saturation voltages of the responsivities is primarily due to the plasmonic effect. In the 2DSHA *n-i-p* device, most EHPs are mainly generated in the absorbing layer near the metal-semiconductor

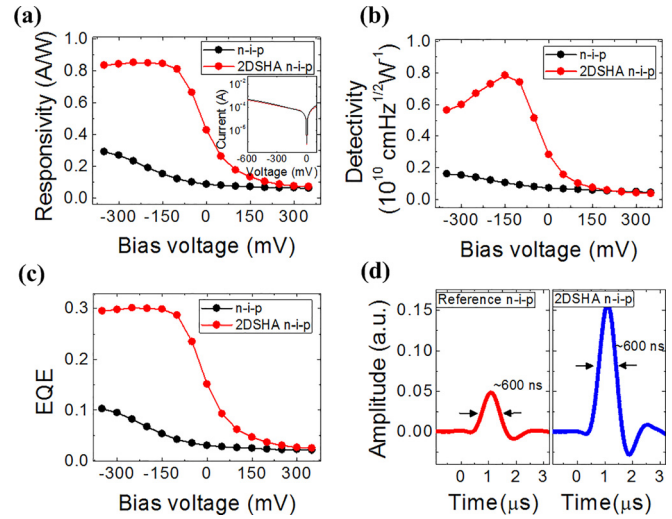


FIG. 5. Room temperature performance of the 2DSHA-hetero *n-i-p* photodiode ($p = 900$ nm) and the reference. (a) Responsivity under biased voltages from -350 mV to 350 mV at room temperature. Inset: room temperature current-voltage characteristics of the photodiodes. (b) Blackbody detectivity at $3.5 \mu\text{m}$. (c) External quantum efficiencies (EQE) at $3.5 \mu\text{m}$. (d) Impulse responses.

interface and the electrons can be fast collected by the electrode. This will lead to a lower bias voltage for the electrons to reach the saturated drift velocity as $v = \mu E$. The room temperature blackbody detectivity ($D = R_i / \sqrt{2qJ + 4kT/(RA)}$, where q is the electronic charge, J is the dark current density, R is the dynamic resistance, A is the area, and R_i is the photo-current responsivity) of the 2DSHA-hetero *n-i-p* photodetector is $0.80 \times 10^{10} \text{ cm Hz}^{1/2} \text{ W}^{-1}$ at -150 mV [Fig. 5(b)], compared to $0.12 \times 10^{10} \text{ cm Hz}^{1/2} \text{ W}^{-1}$ of the reference under the same bias voltage, corresponding to $6.6\times$ enhancement. The external (EQE) quantum efficiencies ($\eta_E = R_i hc / (\lambda q)$, where h is the Planck constant, c is the speed of light in vacuum, q is the element charge, and λ is the wavelength) at $3.5 \mu\text{m}$ are presented in Fig. 5(c) with the maximum value of 30% occurring at -150 mV, corresponding to about $5\times$ enhancement. It is noted that the EQE for the reference device is only $\sim 2\%$ at zero bias, which may due to the barriers in the hetero *n-i-p* structure. We also measured the line widths of the impulse responses²⁸ of the 2DSHA-hetero *n-i-p* device and the reference at zero bias with a $4.77 \mu\text{m}$ quantum cascade laser (QCL) pulse (200 ns in width). They are 600 ns for both devices [Fig. 5(d)], demonstrating a fast response to the input signal. These measured results show that the performance of the 2DSHA-hetero *n-i-p* photodetector can be improved a lot without sacrifice of the speed.

In summary, metallic subwavelength hole array enhanced InAs_{0.91}Sb_{0.09} based heterojunction *n-i-p* photodetectors have been realized, and a room temperature detectivity of $0.8 \times 10^{10} \text{ cm Hz}^{1/2} \text{ W}^{-1}$ has been achieved with a response speed of 600 ns. This work opens a way of developing high sensitivity room temperature MWIR photodetectors with high detectivity meanwhile not reduced response speed. The realization of a room temperature mid-wave infrared photodetector makes the application systems more economic and easily extended to more application domains.

The authors thank Dr. Jean-Luc Reverchon and Dr. Philippe Bois of III-V lab France for their kind support and

help and Professor Wang Qijie, Dr. Guozheng Liang, and Dr. Meng Bo for their assistance. This work was supported by the Economic Development Board (NRF2013SAS-SRP001-019), the Ministry of Education (RG86/13), and AOARD (FA2386-17-1-0039).

- ¹J. M. Martin, J. L. Hernández, L. Adell, A. Rodriguez, and F. López, *Semicond. Sci. Technol.* **11**, 1740 (1996).
- ²Y. Wei, A. Hood, H. Yau, A. Gin, M. Razeghi, M. Z. Tidrow, and V. Nathan, *Appl. Phys. Lett.* **86**, 233106 (2005).
- ³N. Gautam, S. Myers, A. V. Barve, B. Klein, E. P. Smith, D. R. Rhiger, L. R. Dawson, and S. Krishna, *Appl. Phys. Lett.* **101**, 021106 (2012).
- ⁴J. A. Nolde, M. Kim, C. S. Kim, E. M. Jackson, C. T. Ellis, J. Abell, O. J. Glembocki, C. L. Canedy, J. G. Tischler, I. Vurgaftman, J. R. Meyer, and E. H. Aifer, *Appl. Phys. Lett.* **106**, 261109 (2015).
- ⁵S. Maimon and G. W. Wicks, *Appl. Phys. Lett.* **89**, 151109 (2006).
- ⁶A. Soibel, C. J. Hill, S. A. Keo, L. Hoglund, R. Rosenberg, R. Kowalczyk, A. Khoshakhlagh, A. Fisher, D. Z.-Y. Ting, and S. D. Gunapala, *Appl. Phys. Lett.* **105**, 23512 (2014).
- ⁷N. Baril, A. Brown, P. Maloney, M. Tidrow, D. Lubyshev, Y. Qui, J. M. Fastenau, A. W. K. Liu, and S. Bandara, *Appl. Phys. Lett.* **109**, 122104 (2016).
- ⁸J. Tong, L. Y. M. Tobing, P. Ni, and D. H. Zhang, *Appl. Surf. Sci.* **427**, 605 (2018).
- ⁹M. Carras, J. L. Reverchon, G. Marre, C. Renard, B. Vinter, X. Marcadet, and V. Berger, *Appl. Phys. Lett.* **87**, 102103 (2005).
- ¹⁰J. Tong, W. Zhou, Y. Qu, Z. Xu, Z. Huang, and D. H. Zhang, *Nat. Commun.* **8**, 1660 (2017).
- ¹¹C. Genet and T. W. Ebbesen, *Nature* **445**, 39 (2007).
- ¹²W. L. Barnes, A. Dereux, and T. W. Ebbesen, *Nature* **424**, 824 (2003).
- ¹³J. A. Schuller, E. S. Barnard, W. Cai, Y. C. Jun, J. S. White, and M. L. Brongersma, *Nat. Mater.* **9**, 368 (2010).
- ¹⁴F. J. Garcia-Vidal, L. Martin-Moreno, T. W. Ebbesen, and L. Kuipers, *Rev. Mod. Phys.* **82**, 729–787 (2010).
- ¹⁵A. I. Yakimov, V. V. Kirienko, V. A. Armbrister, A. A. Bloshkin, and A. V. Dvurechenskii, *Appl. Phys. Lett.* **112**, 171107 (2018).
- ¹⁶C.-C. Chang, Y. D. Sharma, Y.-S. Kim, J. A. Bur, R. V. Sheno, S. Krishna, D. Huang, and S.-Y. Lin, *Nano Lett.* **10**, 1704 (2010).
- ¹⁷S. J. Lee, Z. Ku, A. Barve, J. Montoya, W.-Y. Jang, S. R. J. Brueck, M. Sundaram, A. Reisinger, S. Krishna, and S. K. Noh, *Nat. Commun.* **2**, 286 (2011).
- ¹⁸G. Gu, J. Vaillancourt, P. Vasinajindakaw, and X. Lu, *Semicond. Sci. Technol.* **28**, 105005 (2013).
- ¹⁹J. A. Kong, *Electromagnetic Wave Theory* (E. M. W. Austin, TX, USA, 2000).
- ²⁰H. Raether, *Surface Plasmons* (Springer, 1988), pp. 5–6.
- ²¹E. D. Palik, *Handbook of Optical Constants of Solids II* (Academic Press, USA, 1991).
- ²²M. A. Ordal, R. J. Bell, R. W. Alexander, L. L. Long, and M. R. Querry, *Appl. Opt.* **24**, 4493 (1985).
- ²³W. L. Barnes, *J. Opt. A Pure Appl. Opt.* **8**, S87 (2006).
- ²⁴H. F. Ghaemi, E. Thip, D. E. Grupp, T. W. Ebbesen, and H. J. Lezec, *Phys. Rev. B* **58**, 6779 (1998).
- ²⁵V. E. Ferry, J. N. Munday, and H. A. Atwater, *Adv. Mater.* **22**, 4794 (2010).
- ²⁶G. Hernandez, *Fabry–Pérot Interferometers* (Cambridge University Press, Cambridge, 1986).
- ²⁷S. M. Sze and K. K. Ng, *Physics of Semiconductor Devices*, 3rd ed. (John Wiley & Sons, New Jersey, 2007).
- ²⁸Y. Gao, H. Cansizoglu, K. G. Polat, S. Ghandiparsi, A. Kaya, H. H. Mamtaz, A. S. Mayet, Y. Wang, X. Zhang, T. Yamada, E. P. Devine, A. F. Elrefaie, S.-Y. Wang, and M. S. Islam, *Nat. Photonics* **11**, 301–308 (2017).